

See discussions, stats, and author profiles for this publication at: <https://www.researchgate.net/publication/47297447>

# Direct Access to Metal or Metal Oxide Nanocrystals Integrated with One-Dimensional Nanoporous Carbons for Electrochemical Energy Storage

ARTICLE in JOURNAL OF THE AMERICAN CHEMICAL SOCIETY · OCTOBER 2010

Impact Factor: 12.11 · DOI: 10.1021/ja106612d · Source: PubMed

CITATIONS

87

READS

30

7 AUTHORS, INCLUDING:



Linjie Zhi

National Center for Nanoscience and Tech...

135 PUBLICATIONS 8,775 CITATIONS

SEE PROFILE



Enrico Mugnaioli

Università degli Studi di Siena

103 PUBLICATIONS 1,142 CITATIONS

SEE PROFILE



U. Kolb

Johannes Gutenberg-Universität Mainz

256 PUBLICATIONS 5,532 CITATIONS

SEE PROFILE

### Direct Access to Metal or Metal Oxide Nanocrystals Integrated with One-Dimensional Nanoporous Carbons for Electrochemical Energy Storage

Yanyu Liang,<sup>†</sup> Matthias Georg Schwab,<sup>†</sup> Linjie Zhi,<sup>‡</sup> Enrico Mugnaioli,<sup>§</sup> Ute Kolb,<sup>§</sup>  
Xinliang Feng,<sup>\*,†</sup> and Klaus Müllen<sup>\*,†</sup>

Max Planck Institute for Polymer Research, Ackermannweg 10, D-55128, Mainz, Germany,  
National Center for Nanoscience and Technology of China, Zhongguancun, Beiyitiao 11,  
100190, Beijing, P. R. China, and Institute of Physical Chemistry, Johannes Gutenberg  
Universität, Welderweg 11, D-55099, Mainz, Germany

Received July 26, 2010; E-mail: feng@mpip-mainz.mpg.de; muellen@mpip-mainz.mpg.de

**Abstract:** Metal and metal oxide nanocrystals have sparked great interest due to their excellent catalytic, magnetic, and electronic properties. Particularly, the integration of metallic nanocrystals and one-dimensional (1D) electronically conducting carbons to form metal–carbon hybrids can lead to enhanced physical and chemical properties or even the creation of new properties with respect to single component materials. However, direct access to thermally stable and structurally ordered 1D metal–carbon hybrids remains a primary challenge. We report an in situ fabrication of Co<sub>3</sub>O<sub>4</sub> or Pt nanocrystals incorporated into 1D nanoporous carbons (NPCs) via an organometallic precursor-controlled thermolysis approach. The AB<sub>2</sub>-type (one diene and two dienophile) 3,4-bis(4-dodecynylphenyl)-substituted cyclopentadienone and its relevant cobalt or platinum complex are first impregnated into the nanochannels of AAO (anodic alumina oxide) membranes. The intermolecular Diels–Alder reaction of these precursor molecules affords the formation of cobalt or platinum functionalized polyphenylene skeletons. Subsequent thermolysis transforms the polyphenylene backbones into 1D nanoporous carbonaceous frameworks, while the metallic moieties are reduced into Co or Pt nanocrystals, respectively. After removal of the AAO template, 1D NPCs/Co<sub>3</sub>O<sub>4</sub> or NPCs/Pt are obtained, for which structural characterizations reveal that high-quality Co<sub>3</sub>O<sub>4</sub> or Pt nanocrystals are distributed homogeneously within carbon frameworks. These unique 1D metal–carbon hybrids exhibit a promising potential in electrochemical energy storage. NPCs/Co<sub>3</sub>O<sub>4</sub> is evaluated as an electrode material in a supercapacitor, for which Co<sub>3</sub>O<sub>4</sub> nanocrystals contribute an exceptionally high gravimetric capacitance value of 1066 F g<sup>−1</sup>. NPCs/Pt is applied as an electrocatalyst showing excellent catalytic efficiency toward methanol oxidation in comparison to commercial E-TEK (Pt/C) catalyst.

#### Introduction

Metal and metal oxide nanocrystals have been extensively studied owing to their unique magnetic, catalytic, and electronic properties across a broad range of fundamental and technological potential.<sup>1,2</sup> In particular, the integration of metallic nanocrystals and one-dimensional (1D) substrate materials to form nanoscale heterostructures has been explored for a variety of applications including biolabeling, chemical sensing, catalysis, and micro-

or nanoelectronics.<sup>3–6</sup> With respect to other substrate materials, 1D carbons such as carbon nanotubes (CNTs) and nanofibers show advantages for growing and anchoring functional metallic nanocrystals in view of their superior physical features including

<sup>†</sup> Max Planck Institute for Polymer Research.

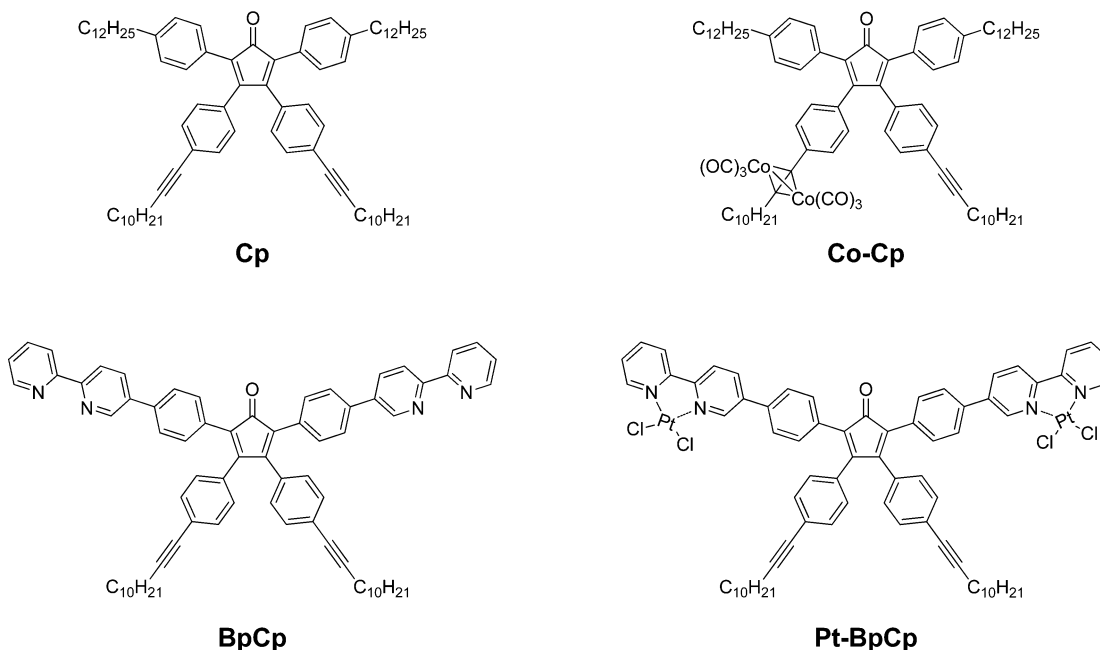
<sup>‡</sup> National Center for Nanoscience and Technology of China.

<sup>§</sup> Johannes Gutenberg Universität.

- (1) (a) Sun, Y. G.; Xia, Y. N. *Science* **2002**, 298, 2176–2179. (b) Tian, N.; Zhou, Z. Y.; Sun, S. G.; Ding, Y.; Wang, Z. L. *Science* **2007**, 316, 732–735. (c) Murray, C. B.; Kagan, C. R.; Bawendi, M. G. *Annu. Rev. Mater. Sci.* **2000**, 30, 545–610. (d) Xia, Y. N.; Yang, P. D.; Sun, Y. G.; Wu, Y. Y.; Mayers, B.; Gates, B.; Yin, Y. D.; Kim, F.; Yan, Y. Q. *Adv. Mater.* **2003**, 15, 353–389. (e) Huang, X. H.; El-Sayed, I. H.; Qian, W.; El-Sayed, M. A. *J. Am. Chem. Soc.* **2006**, 128, 2115–2120.
- (2) (a) Cozzoli, P. D.; Kornowski, A.; Weller, H. *J. Am. Chem. Soc.* **2003**, 125, 14539–14548. (b) Jun, Y. W.; Choi, J. S.; Cheon, J. *Angew. Chem., Int. Ed.* **2006**, 45, 3414–3439. (c) Park, J.; An, K. J.; Hwang, Y. S.; Park, J. G.; Noh, H. J.; Kim, J. Y.; Park, J. H.; Hwang, N. M.; Hyeon, T. *Nat. Mater.* **2004**, 3, 891–895.

- (3) (a) Kundu, P.; Halder, A.; Viswanath, B.; Kundu, D.; Ramanath, G.; Ravishanker, N. *J. Am. Chem. Soc.* **2010**, 132, 20–21. (b) Menagen, G.; Macdonald, J. E.; Shemesh, Y.; Popov, I.; Banin, U. *J. Am. Chem. Soc.* **2009**, 131, 17406–17411. (c) Wu, Y.; Xiang, J.; Yang, C.; Lu, W.; Lieber, C. M. *Nature* **2004**, 430, 61–65. (d) Yan, W. F.; Brown, S.; Pan, Z. W.; Mahurin, S. M.; Overbury, S. H.; Dai, S. *Angew. Chem., Int. Ed.* **2006**, 45, 3614–3618. (e) Yan, W. F.; Mahurin, S. M.; Pan, Z. W.; Overbury, S. H.; Dai, S. *J. Am. Chem. Soc.* **2005**, 127, 10480–10481.
- (4) (a) Zong, Z. C.; Liu, J. Y.; Hu, T. T.; Li, D. D.; Tian, H. F.; Liu, C.; Zhang, M. Z.; Zou, G. T. *Nanotechnology* **2010**, 21, 185302. (b) Zong, Z. C.; Zhang, M. Z.; Lu, H. L.; Xu, D.; Wang, S. M.; Tian, H. F.; Liu, C.; Guo, H. M.; Gao, H. J.; Zou, G. T. *Appl. Phys. Lett.* **2010**, 96, 143113.
- (5) (a) Guo, S. J.; Dong, S. J.; Wang, E. K. *Adv. Mater.* **2010**, 22, 1269–1272. (b) Han, L.; Wu, W.; Kirk, F. L.; Luo, J.; Maye, M. M.; Kariuki, N. N.; Lin, Y. H.; Wang, C. M.; Zhong, C. J. *Langmuir* **2004**, 20, 6019–6025. (c) Liu, Z. L.; Lin, X. H.; Lee, J. Y.; Zhang, W.; Han, M.; Gan, L. M. *Langmuir* **2002**, 18, 4054–4060. (d) Ellis, A. V.; Vjayamohan, K.; Goswami, R.; Chakrapani, N.; Ramanathan, L. S.; Ajayan, P. M.; Ramanath, G. *Nano Lett.* **2003**, 3, 279–282. (e) Tang, Z. Y.; Kotov, N. A. *Adv. Mater.* **2005**, 17, 951–962.

**Scheme 1.** Chemical Structure of the Four Precursors for the Fabrication of NPCs/Co<sub>3</sub>O<sub>4</sub> and NPCs/Pt respectively: Cp, Co-Cp, BpCp, and Pt-BpCp



high surface area, mechanical strength, and thermal stability.<sup>7</sup> When appropriate metallic nanocrystals are incorporated into 1D electronically conducting carbons to form metal–carbon hybrids, unprecedented physical and chemical properties become available due to the effects of spatial confinement and synergetic electronic interactions between metallic and carbonaceous components.<sup>5,6,8</sup>

In general, two well-established synthetic protocols have been put forward for the fabrication of 1D metal–carbon hybrids: (1) preformed metallic nanocrystals are connected to functionalized 1D carbon frameworks via either covalent or noncovalent interactions; and (2) naked metallic nanocrystals are directly grown or deposited onto the surface of 1D carbons through chemical reduction processes. For the first strategy, strong acid assisted functionalization treatments are generally involved which unavoidably introduce a large number of defect sites into 1D carbons, leading to the disruption of their intrinsic electronic and mechanical properties.<sup>5,9</sup> The second approach is attractive toward creating 1D metal–carbon hybrids; however, the absence of functional units renders it impossible to uniformly distribute metallic nanocrystals onto 1D carbons.<sup>6,10</sup> In addition, the involvement of multiple and tedious synthetic steps in both methods limits experimental simplicity, not to mention that the agglomeration of metallic nanocrystals often occurs in their synthesis. Although few reports on thermal decomposition of commercially available organometallic complexes have been demonstrated to achieve 1D metal–carbon hybrids, they suffer from poor structural order owing to the difficulties in controlling the nucleation and growth of metallic nanocrystals.<sup>11,12</sup> Therefore, establishing an efficient and facile synthesis protocol for the homogeneous distribution of metallic nanocrystals into 1D carbon frameworks remains a great challenge.<sup>13</sup>

In this article, we present a novel strategy for in situ fabrication of metallic nanocrystals integrated with 1D nanoporous carbons (NPCs) via an organometallic precursor-controlled thermolysis. The synthetic procedure typically involves the impregnation of precursor molecules into inorganic nanochannels of anodic alumina oxide (AAO) membranes followed by

solid-state thermal treatment. The AB<sub>2</sub>-type (one diene and two dienophile) 3,4-bis(4-dodecynylphenyl)-2,5-bis(4-dodecylphenyl) cyclopentadienone (Cp, Scheme 1) and its corresponding dicobalt hexacarbonyl complex (Co-Cp, Scheme 1) serve as

- (6) (a) Choi, H. C.; Shim, M.; Bangsaruntip, S.; Dai, H. *J. Am. Chem. Soc.* **2002**, *124*, 9058–9059. (b) Quinn, B. M.; Dekker, C.; Lemay, S. G. *J. Am. Chem. Soc.* **2005**, *127*, 6146–6147. (c) Qu, L. T.; Dai, L. M. *J. Am. Chem. Soc.* **2005**, *127*, 10806–10807. (d) Qu, L. T.; Dai, L. M.; Osawa, E. *J. Am. Chem. Soc.* **2006**, *128*, 5523–5532.
- (7) (a) Baughman, R. H.; Zakhidov, A. A.; Heer, W. A. *Science* **2002**, *297*, 787–792. (b) Fan, S.; Chapline, M. G.; Franklin, N. R.; Tomblar, T. W.; Cassell, A. M.; Dai, H. *Science* **1999**, *283*, 512–514. (c) Kong, J.; Franklin, N. R.; Zhou, C. W.; Chapline, M. G.; Peng, S.; Cho, H. J.; Dai, H. *Science* **2000**, *287*, 622–625.
- (8) (a) Kong, J.; Chapline, M. G.; Dai, H. *Adv. Mater.* **2001**, *13*, 1384–1386. (b) Banerjee, S.; Wong, S. S. *Nano Lett.* **2002**, *2*, 195–200. (c) Mieszwaska, A. J.; Jalilian, R.; Sumanasekera, G. U.; Zamborini, F. P. *Small* **2007**, *3*, 722–756. (d) Luo, J.; Zhu, J. *Nanotechnology* **2006**, *17*, S262–S270. (e) Peng, X. H.; Chen, J. Y.; Misewich, J. A.; Wong, S. S. *Chem. Soc. Rev.* **2009**, *38*, 1076–1098. (f) Georgakilas, V.; Gournis, D.; Tzitzios, V.; Pasquato, L.; Guldi, D. M.; Prato, M. *J. Mater. Chem.* **2007**, *17*, 2679–2694.
- (9) (a) Coleman, K. S.; Bailey, S. R.; Fogden, S.; Green, M. L. H. *J. Am. Chem. Soc.* **2003**, *125*, 8722–8723. (b) Jiang, K. Y.; Eitan, A.; Schadler, L. S.; Ajayan, P. M.; Siegel, R. W.; Grobert, N.; Mayne, M.; Reyes-Reyes, M.; Terrones, H.; Terrones, M. *Nano Lett.* **2003**, *3*, 275–277.
- (10) (a) Mu, Y. Y.; Liang, H. P.; Hu, S. H.; Jiang, L.; Wan, L. J. *J. Phys. Chem. B* **2005**, *109*, 22212–22216. (b) Kong, B. S.; Jung, D. H.; Oh, S. K.; Han, C. S.; Jung, H. T. *J. Phys. Chem. C* **2007**, *111*, 8377–8382.
- (11) (a) Laskoski, M.; Steffen, W.; Morton, J. G. M.; Smith, M. D.; Bunz, U. H. F. *J. Am. Chem. Soc.* **2002**, *124*, 13814–13818. (b) Walter, E. C.; Beetz, T.; Sfeir, M. Y.; Brus, L. E.; Steigerwald, M. L. *J. Am. Chem. Soc.* **2006**, *128*, 15590–15591. (c) Zhu, H. G.; Liang, C. D.; Yan, W. F.; Overbury, S. H.; Dai, S. J. *Phys. Chem. B* **2006**, *110*, 10842–10848.
- (12) (a) Ciuculescu, D.; Dumestre, F.; Comesañá-Hermo, M.; Chaudret, B.; Spasova, M.; Farle, M.; Amiens, C. *Chem. Mater.* **2009**, *21*, 3987–3995. (b) Juárez, B. H.; Klinke, C.; Kornoeski, A.; Weller, H. *Nano Lett.* **2007**, *7*, 3564–3568.
- (13) (a) Lu, C. G.; Akey, A.; Wang, W.; Herman, I. P. *J. Am. Chem. Soc.* **2009**, *131*, 3446–3447. (b) Kundu, P.; Halder, A.; Viswanath, B.; Kundu, D.; Ramanath, G.; Ravishankar, N. *J. Am. Chem. Soc.* **2010**, *132*, 20–21. (c) Goring, P.; Pippel, E.; Hofmeister, H.; Wehrspohn, R. B.; Steinhart, M.; Gosele, U. *Nano Lett.* **2004**, *4*, 1121–1125.

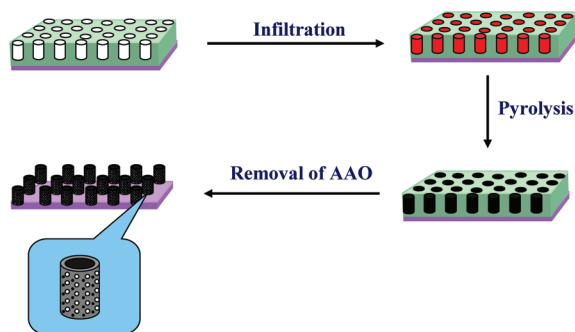


**Figure 1.** Schematic illustration of the preparation of 1D NPCs/Co<sub>3</sub>O<sub>4</sub> or NPCs/Pt.

molecular precursors for the buildup of cobalt functionalized polyphenylene skeletons via Diels–Alder polymerization, which are transformed into NPCs with the incorporation of Co<sub>3</sub>O<sub>4</sub> nanocrystals (NPCs/Co<sub>3</sub>O<sub>4</sub>) after further thermolysis. Similarly, 3,4-bis(4-dodecynylphenyl)-2,5-bis(4-(2,2′-bipyridyl)phenyl) cyclopentadienone (BpCp, Scheme 1) and its corresponding platinum dichloride complex (Pt-BpCp, Scheme 1) are chosen for the synthesis of NPCs integrated with Pt nanocrystals (NPCs/Pt). After removal of the AAO template, these novel 1D metal–carbon hybrids are further evaluated in electrochemical energy storage. Remarkably, the as-prepared NPCs/Co<sub>3</sub>O<sub>4</sub> and NPCs/Pt show superior electrochemical performances as active electrode materials in supercapacitor and fuel cell devices, respectively.

## Experimental Section

**Synthesis.** The synthesis of Cp bearing two dodecynyl groups has been reported previously.<sup>14</sup> It has been shown that the intermolecular Diels–Alder cycloaddition reaction between alkynyl and cyclopentadienone moieties in the skeleton of Cp is an efficient method for the generation of polyphenylene structures.<sup>14</sup> One of the two alkynyl functions was further transformed into a dicobalt hexacarbonyl metal complex by treatment with dicobalt octacarbonyl Co<sub>2</sub>(CO)<sub>8</sub>, giving rise to the formation of Co-Cp (Figure S1).<sup>14b</sup> Another precursor compound, BpCp containing 2,2′-bipyridyl moieties, was prepared according to the synthetic route shown in Scheme S1. A complex of Pt-BpCp was then obtained by the coordination reaction of BpCp with potassium tetrachloroplatinate K<sub>2</sub>PtCl<sub>4</sub> (Figure S2).<sup>15</sup>

First, the precursors of Cp and Co-Cp or BpCp and Pt-BpCp were impregnated into the nanochannels of AAO membranes (Whatman International Ltd. with an average pore diameter of 200 nm). Heat treatment of the precursors in the confined channels at 150 °C generated cobalt or platinum functionalized polyphenylene frameworks.<sup>14a,16</sup> Subsequently, the samples were treated at 350 °C for 5 h under an argon atmosphere followed by thermolysis at 700 °C for 1 h. After the removal of the AAO template in a 3 M NaOH solution, NPCs/Co<sub>3</sub>O<sub>4</sub> or NPCs/Pt was obtained respectively (Figure 1).

**Characterization.** For transmission electron microscopy (TEM) and high-resolution transmission electron microscopy (HRTEM) investigations, the samples were sprayed onto holey carbon coated copper grids using the procedure described elsewhere.<sup>17</sup> TEM and HRTEM characterizations were carried out on Tecnai F30 and Tecnai F20 transmission electron microscopes (Philips, FEI, TECNAI), both equipped with a field emission gun and working at 200 and 300 kV respectively. Nanoelectron diffraction (NED) patterns were acquired with a 10 C<sup>2</sup> aperture, and the beam diameter was approximately 30 nm. TIA (TEM Imaging & Analysis) software was used for Energy dispersive X-ray (EDX) analysis. For scanning transmission electron microscopy (STEM), a high angular annular dark field (HAADF) detector was applied to enhance the contrast. Fourier transform infrared (FTIR) spectra were recorded with a Nicolet 730 FTIR spectrometer. Thermal gravimetric analysis (TGA) was performed on a Mettler TGA/SDTA 851e thermobalance at a heating rate of 10 K min<sup>−1</sup>.

Electrochemical experiments were conducted on an EG&G potentiostat/galvanostat Model 2273 instrument. A conventional cell with a three-electrode configuration was used throughout the study. For a supercapacitor device, a working electrode was prepared by mixing NPCs/Co<sub>3</sub>O<sub>4</sub> with carbon black (Mitsubishi Chemicals, Inc.) and polytetrafluoroethylene (PTFE) binder. The weight ratio of these three components was 80:10:10. For a fuel cell device, a working electrode was prepared by a procedure described elsewhere.<sup>18</sup> Briefly, 5 mg of as-prepared NPCs/Pt or commercially available E-TEK (Pt/C) were dispersed in 1 mL of 0.05 wt % Nafion solution by ultrasonication treatment for 5 min. Then a 25 μL aliquot of the dispersion was transferred onto a mirror-polished glassy carbon electrode. In these two devices, a platinum foil was applied as a counter electrode with a standard calomel electrode (SCE) as a reference electrode.

## Results and Discussion

**Structural Characterizations.** FTIR spectroscopy and differential scanning calorimetry (DSC, measured from 20 to 200 °C) were employed to investigate intermolecular Diels–Alder cycloaddition reactions for Cp and Co-Cp or BpCp and Pt-BpCp. Both DSC curves (Cp and Co-Cp or BpCp and Pt-BpCp) disclose an exothermal peak at around 150 °C, attributable to the Diels–Alder reaction between cyclopentadienone and alkyne moieties (Figure S3). Figure 2a shows the FTIR spectra of the Cp and Co-Cp mixture before and after the DSC measurement, respectively. Three sharp peaks centered at 2084, 2045, and 2013 cm<sup>−1</sup> can be assigned to the terminal carbonyl groups presented in the skeleton of Co-Cp, in agreement with values reported in the literature.<sup>19</sup> The peak at the wavenumber 1711 cm<sup>−1</sup> can be assigned to the stretching vibration of the C=O group in the cyclopentadienone moiety.<sup>20</sup> After the heat treatment, the bands in the range of 2013–2084 cm<sup>−1</sup> are no longer detected, while the peak corresponding to the carbonyl vibration significantly decreases in intensity. A similar result can be observed in the FTIR spectra of BpCp and Pt-BpCp before and after the DSC measurement (Figure 2b). In fact, after the heating procedure described above, the products are no longer soluble in normal organic solvents. In association with the MALDI-TOF mass spectra showing no detectable peaks, these results suggest a successful intermolecular cross-linking process<sup>14a,16</sup> of Cp and

- (14) (a) Zhi, L.; Wu, J.; Li, J.; Stepputat, M.; Kolb, U.; Müllen, K. *Adv. Mater.* **2005**, *17*, 1492–1496. (b) Hamaoui, B. E.; Zhi, L.; Wu, J.; Li, J.; Lucas, N. T.; Tomović, Z.; Kolb, U.; Müllen, K. *Adv. Funct. Mater.* **2007**, *17*, 1179–1187. (c) Stumpe, K.; Komber, H.; Voit, B. I. *Macromol. Chem. Phys.* **2006**, *207*, 1825–1833. (d) Komber, H.; Stumpe, K.; Voit, B. I. *Macromol. Chem. Phys.* **2006**, *207*, 1814–1824.
- (15) Smith, A. P.; Fraser, C. L. *Macromolecules* **2002**, *35*, 594–596.
- (16) (a) Cui, G. L.; Zhi, L. J.; Thomas, A.; Kolb, U.; Lieberwirth, I.; Müllen, K. *Angew. Chem., Int. Ed.* **2007**, *46*, 3464–3467. (b) Zhi, L. J.; Wang, J. J.; Cui, G. L.; Kastler, M.; Schmaltz, B.; Kolb, U.; Jonas, U.; Müllen, K. *Adv. Mater.* **2007**, *19*, 1849–1853. (c) Liang, Y. Y.; Feng, X. L.; Zhi, L. J.; Kolb, U.; Müllen, K. *Chem. Commun.* **2009**, 809–811.

- (17) Mugnaioli, E.; Gorelik, T.; Kolb, U. *Ultramicroscopy* **2009**, *6*, 758–765.
- (18) Schmidt, T. J.; Gasteiger, H. A.; Staeb, G. D.; Urban, P. M.; Kolb, D. M.; Behm, R. J. *J. Electrochem. Soc.* **1998**, *145*, 2354–2358.
- (19) Greenfield, H.; Sternberg, H. W.; Friedel, R. A.; Wotiz, J. H.; Markby, R.; Wender, I. *J. Am. Chem. Soc.* **1956**, *78*, 120–124.
- (20) Liang, Y. Y.; Wu, D. Q.; Feng, X. L.; Müllen, K. *Adv. Mater.* **2009**, *21*, 1679–1684.



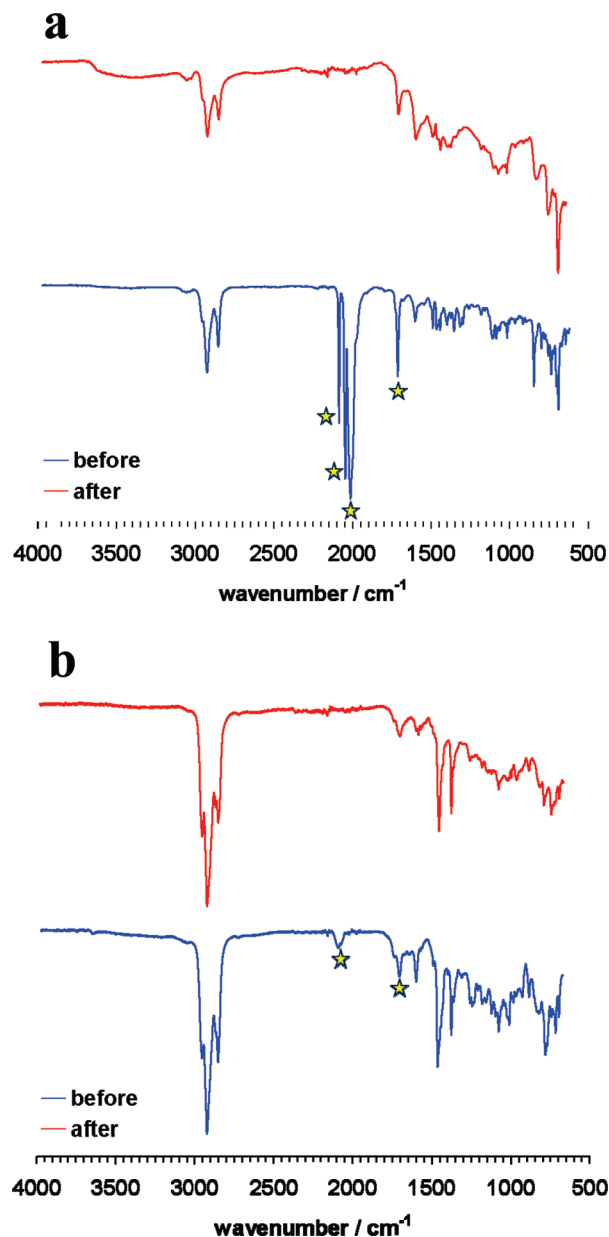


**Figure 2.** FTIR spectra of (a) Cp and Co-Cp before and after the DSC measurement; (b) BpCp and Pt-BpCp before and after the DSC measurement. Stars indicate the terminal carbonyl, alkynyl, and C=O group of the cyclopentadienone, respectively. For better comparison of the intensities, all spectra were normalized to the band at  $2930\text{ cm}^{-1}$ .

Co-Cp or BpCp and Pt-BpCp leading to the formation of cobalt or platinum functionalized polyphenylene backbones (Figure S3).

Further heat treatment at  $350\text{ }^{\circ}\text{C}$  for 5 h is expected to promote completion of the Diels–Alder reactions, affording a more rigid polyphenylene skeleton within the AAO membranes.<sup>14a,16</sup> Subsequently, the samples are treated at  $700\text{ }^{\circ}\text{C}$  under an argon atmosphere, allowing the transformation of the polyphenylene backbones into carbonaceous frameworks in the membrane channels, while the metallic moieties in the precursor of Co-Cp or Pt-BpCp can be reduced into Co or Pt nanocrystals, respectively. After the removal of the AAO template in a 3 M NaOH solution, NPCs/ $\text{Co}_3\text{O}_4$ <sup>21</sup> and NPCs/Pt are achieved (see below discussion for detailed structural characterizations).

As demonstrated in Figure S4, a large-scale STEM image reveals that NPCs/ $\text{Co}_3\text{O}_4$  comprises 1D materials with an

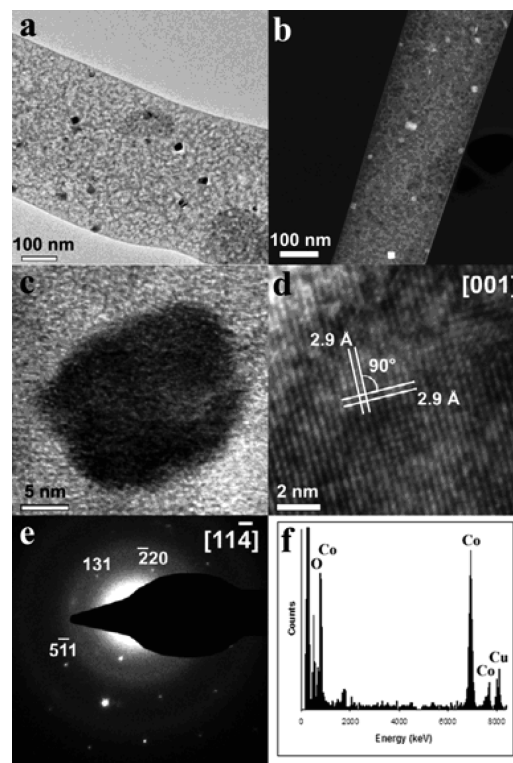


**Figure 3.** (a and b) TEM and STEM (dark field) images of NPCs/ $\text{Co}_3\text{O}_4$  show 1D nanoporous carbons and well-dispersed  $\text{Co}_3\text{O}_4$  nanocrystals with sharp edges. (c) HRTEM image of a  $\text{Co}_3\text{O}_4$  nanocrystal. (d) HRTEM image of a  $\text{Co}_3\text{O}_4$  nanocrystal oriented along  $[001]$ ; the orthogonal  $(220)$  and  $(2-20)$  lattice fringes are drawn. (e) NED pattern of a  $\text{Co}_3\text{O}_4$  nanocrystal oriented along  $[11-4]$  indicates that it is single crystalline cubic  $\text{Co}_3\text{O}_4$ . (f) EDX shows the presence of both O and Co peaks.

average diameter of 200–500 nm and a length of a few micrometers. On the basis of Brunauer–Emmett–Teller (BET)<sup>16</sup> and TEM studies (Figure 3a and b), the carbonaceous frameworks possess a nanoporous structure with a pore diameter ranging from 1 to 20 nm. High-contrast  $\text{Co}_3\text{O}_4$  nanoparticles with a size of 10 to 30 nm and sharp edges are homogeneously distributed within these carbon textures (Figure 3a and b). HRTEM and NED experiments further disclose that these cobalt nanoparticles are single crystalline face-centered cubic  $\text{Co}_3\text{O}_4$  ( $a = 8.1\text{ }\text{\AA}$ , space group of  $Fd\bar{3}m$ , No. 227, Figure 3c–e). Common lattice distances of 4.7, 4.1, 2.9, and  $2.4\text{ }\text{\AA}$  correspond to  $\{111\}$ ,  $\{200\}$ ,  $\{220\}$ , and  $\{311\}$  planes, respectively. EDX spectroscopy detects both the peaks of O and Co (Figure 3f). In fact, the initially synthesized metallic nanocrystals are cobalt as indicated by the X-ray diffraction (Figure S6). The formation of cobalt oxide after the removal of the AAO template can be attributed to the long-time impregnation in concentrated NaOH solution which results in the external surface oxidation of Co into  $\text{Co}_3\text{O}_4$ .<sup>22</sup>

To enhance the degree of crystallinity of the above synthesized  $\text{Co}_3\text{O}_4$  nanocrystals, the as-prepared NPCs/ $\text{Co}_3\text{O}_4$  is further annealed at  $400\text{ }^{\circ}\text{C}$  in air for 10 min. The morphology of NPCs is preserved, whereas the optical contrast shown in Figure 4a is lower than that of the nonoxidized form. The generated  $\text{Co}_3\text{O}_4$

(21) The external metallic cobalt nanoparticles can be oxidized into cobalt oxide during the removal of the AAO template process; see detailed discussion and Figure S6.

(22) (a) Tzvetkoff, T.; Girginov, A.; Bojinov, M. *J. Mater. Sci.* **1995**, *30*, 5561–5575. (b) Gencheva, Tzvetkoff, R. T.; Bojinov, M. *Appl. Surf. Sci.* **2004**, *241*, 459–470.

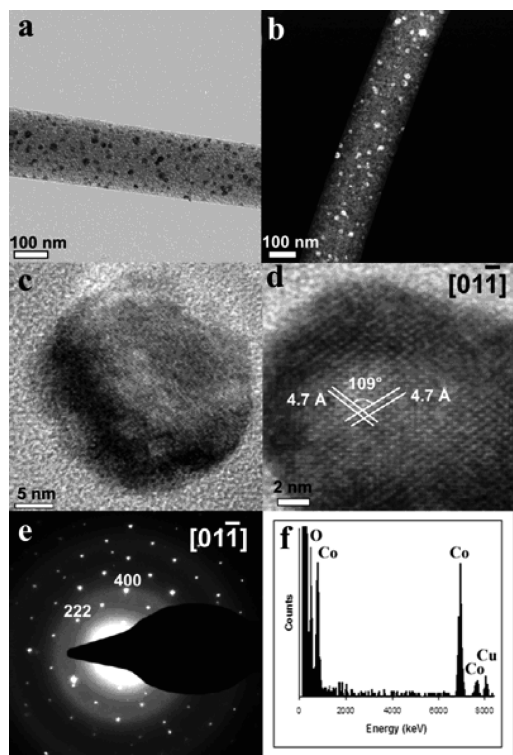


**Figure 4.** (a and b) TEM and STEM (dark field) images of NPCs/Co<sub>3</sub>O<sub>4</sub> after oxidation treatment show 1D nanoporous carbons and the well-dispersed Co<sub>3</sub>O<sub>4</sub> nanocrystals with rounded shape. (c) HRTEM image of a Co<sub>3</sub>O<sub>4</sub> nanocrystal. (d) HRTEM image of a Co<sub>3</sub>O<sub>4</sub> nanocrystal oriented along [01-1]; the two lattice fringe sets (111) and (1-1-1) are drawn. (e) NED pattern of a Co<sub>3</sub>O<sub>4</sub> nanocrystal oriented along [01-1] indicates that it is single crystalline cubic Co<sub>3</sub>O<sub>4</sub>. (f) EDX shows the presence of both O and Co peaks.

nanocrystals exhibit smooth edges with a size of 20 to 40 nm, which is larger than that of the nonoxidized counterpart. It is noted that most Co<sub>3</sub>O<sub>4</sub> nanocrystals (more than 90%) reveal a well-ordered single crystalline nature with a weak contrast at the core of the nanoparticles, suggesting the formation of a hollow structure after additional oxidation treatment (Figure 4b and c). Such a novel morphological evolution can be rationally ascribed to the well-known Kirkendall effect.<sup>23</sup> All of the NED patterns are well consistent with the face-centered cubic Co<sub>3</sub>O<sub>4</sub> single crystals with  $a = 8.1 \text{ \AA}$  (Figure 4d, e). The oxygen content in NPCs/Co<sub>3</sub>O<sub>4</sub> is greatly increased relative to that of the nonoxidized counterpart (Figure 4f). It is therefore reasonable to conclude that the additional thermal annealing in air leads to a complete oxidation of the Co species with the formation of larger hollow Co<sub>3</sub>O<sub>4</sub> nanocrystals.

Similarly, NPCs/Pt is first examined by TEM characterization after the removal of the AAO template. In Figure 5a and b, Pt nanoparticles with an average diameter of 2 to 6 nm are homogeneously distributed into carbon frameworks. HRTEM images (Figure 5c–e) reveal that the metallic phase is composed of Pt single crystals ( $a = 3.9 \text{ \AA}$ , space group  $Fm\bar{3}m$ , No. 225). In accordance with NED patterns (Figure 5f), the only crystalline phase presented in NPCs/Pt is metallic platinum showing high resolution lattice fringes of {111}, {200}, {220}, and {311}, respectively. EDX analysis confirms both the C and Pt components (Figure 5g). Additional peaks for Cu and O can be attributed to the underlying copper grid.

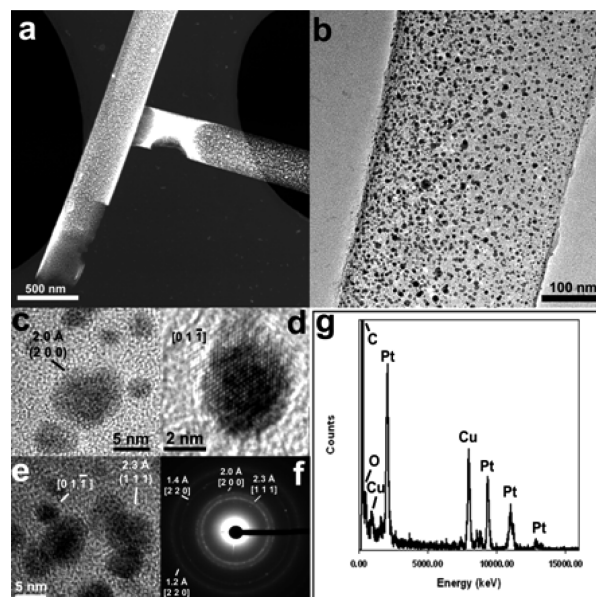


**Figure 5.** (a) STEM image of NPCs/Pt (dark field) overview shows the typical tubular feature of the carbons. (b) TEM image of NPCs/Pt discloses the homogeneously dispersed platinum nanocrystals on 1D carbon substrates with rounded shape. (c–e) HRTEM images of different oriented platinum nanocrystals demonstrate that each particle is a single crystal. (f) NED patterns show that the only crystalline phase is metallic Pt. (g) EDX reveals both C and Pt peaks and a small O peak possibly coming from the Cu grid.

**Electrochemical Properties.** The good dispersion of metallic nanocrystals<sup>24</sup> within 1D nanoporous carbon frameworks indicates that the as-synthesized NPCs/Co<sub>3</sub>O<sub>4</sub> and NPCs/Pt are promising electrode materials for electrochemical energy storage.<sup>25</sup> As a typical example, NPCs/Co<sub>3</sub>O<sub>4</sub> is evaluated in an electrochemical capacitor device after additional oxidation. For comparison, conventional multiwalled carbon nanotube supported polycrystalline Co<sub>3</sub>O<sub>4</sub> nanoparticles (CNTs/Co<sub>3</sub>O<sub>4</sub>, preparation procedure can be found in the Supporting Information) with the same mass loading of cobalt species were also investigated under the same experimental conditions. Figure 6a presents representative cyclic voltammograms (CV) measured at a scan rate of 10 and 50 mV s<sup>-1</sup> for both NPCs/Co<sub>3</sub>O<sub>4</sub> and CNTs/Co<sub>3</sub>O<sub>4</sub>, respectively. None of the CV curves exhibits a symmetrical rectangular shape, indicating that pseudocapacitance originating from the electrochemically active Co<sub>3</sub>O<sub>4</sub> component is dominant in the whole capacitance. This asymmetrical CV curve is more prominent in the case of NPCs/Co<sub>3</sub>O<sub>4</sub> at a scan rate of 50 mV s<sup>-1</sup>, revealing that single-crystalline Co<sub>3</sub>O<sub>4</sub> exhibits a better high-rate response than that of the polycrys-

(23) Yin, Y. D.; Rioux, R. M.; Erdonmez, C. K.; Hughes, S.; Somorjai, G. A.; Alivisatos, A. P. *Science* **2004**, *30*, 711–714.

(24) (a) Nam, K. M.; Shim, J. H.; Ki, H.; Choi, S.; Lee, G.; Jang, J. K.; Jo, Y.; Jung, M.-H.; Song, H.; Park, J. T. *Angew. Chem., Int. Ed.* **2008**, *47*, 9504–9508. (b) Hu, L.; Peng, Q.; Li, Y. *J. Am. Chem. Soc.* **2008**, *130*, 16136–16137. (c) Tian, B.; Liu, X.; Solovyov, L. A.; Liu, Z.; Yang, H.; Zhang, Z.; Xie, S.; Zhang, F.; Tu, B.; Yu, C.; Terasaki, O.; Zhao, D. *J. Am. Chem. Soc.* **2004**, *126*, 865–875. (d) Kim, D. K.; Muralidharan, P.; Lee, H. W.; Ruffo, R.; Yang, Y. C.; Chan, K.; Peng, H. L.; Huggins, R. A.; Cui, Y. *Nano Lett.* **2008**, *8*, 3948–3952. (25) (a) Reddy, A. L. M.; Ramaprabhu, S. *J. Phys. Chem. C* **2007**, *111*, 7727–7734. (b) Kongkanand, A.; Dominguez, R. M.; Kamat, P. V. *Nano Lett.* **2007**, *7*, 676–680. (c) Simon, P.; Gogotsi, A. Y. *Nat. Mater.* **2008**, *7*, 845–854. (d) Arico, A. S.; Bruce, P.; Scrosati, B.; Tarascon, J. M.; van Schalkwijk, W. *Nat. Mater.* **2005**, *4*, 366–377. (e) Lee, J.; Kim, J.; Hyeon, T. *Adv. Mater.* **2006**, *18*, 2073–2094. (f) Wasmus, S.; Kuver, A. *J. Electroanal. Chem.* **1999**, *461*, 14–31. (g) Periana, R. A.; Taube, D. J.; Gamble, S.; Taube, H.; Satoh, T.; Fujii, H. *Science* **1998**, *280*, 560–564.

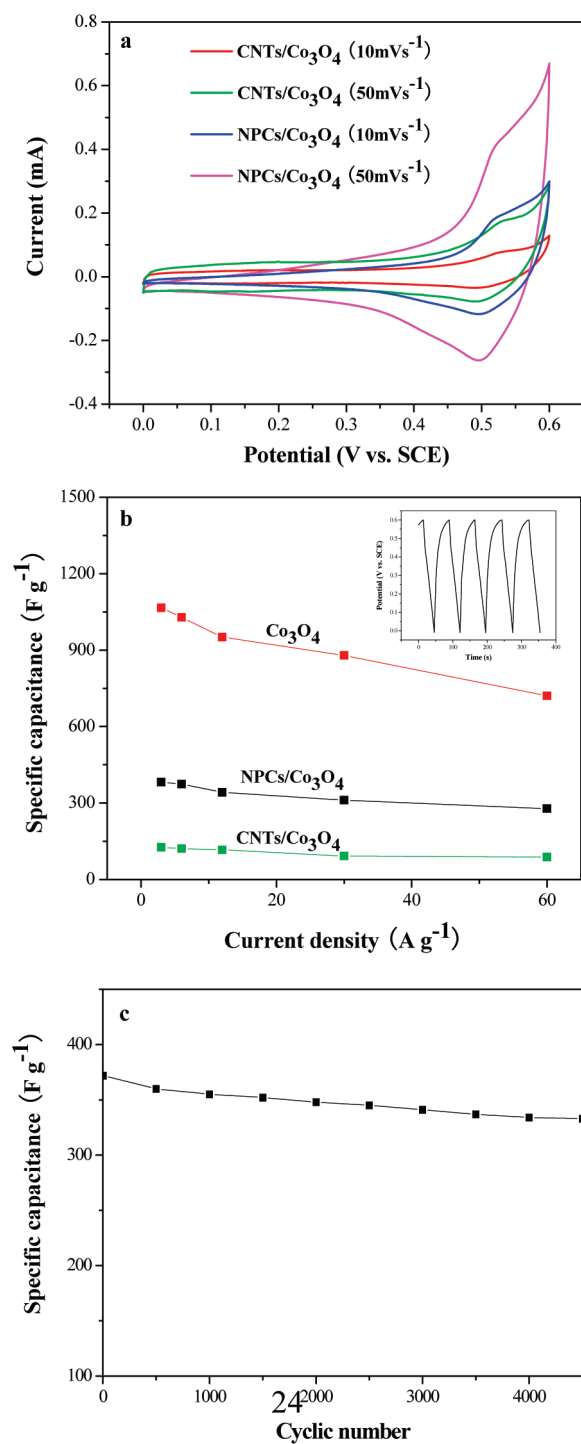


**Figure 6.** (a) Cyclic voltammograms of NPCs/Co<sub>3</sub>O<sub>4</sub> and CNTs/Co<sub>3</sub>O<sub>4</sub> at sweep rates of 10 and 50 mV s<sup>-1</sup> in 1 M KOH electrolyte. (b) The specific capacitance versus the current density for NPCs/Co<sub>3</sub>O<sub>4</sub>, Co<sub>3</sub>O<sub>4</sub>, and CNTs/Co<sub>3</sub>O<sub>4</sub>, respectively (inset: the charge and discharge curves of NPCs/Co<sub>3</sub>O<sub>4</sub> at the density of 6 A g<sup>-1</sup>). (c) The evolution of the specific capacitance versus the number of cycles for NPCs/Co<sub>3</sub>O<sub>4</sub>.

talline counterpart in CNTs/Co<sub>3</sub>O<sub>4</sub>. Galvanostatic charge–discharge measurements were applied to investigate the capacitive performance at a set of current densities ranging from 3 to 60 A g<sup>-1</sup>. The calculated specific capacitance of NPCs/Co<sub>3</sub>O<sub>4</sub> at a current rate of 3, 6, 12, 30, and 60 A g<sup>-1</sup> is 382, 374, 342, 311, and 278 F g<sup>-1</sup>, respectively (Figure 6b). Taking the current density of 3 A g<sup>-1</sup> as an example, the specific capacitance of NPCs/Co<sub>3</sub>O<sub>4</sub> is 382 F g<sup>-1</sup>, much higher than that of CNTs/Co<sub>3</sub>O<sub>4</sub>

(126 F g<sup>-1</sup>). Even under high current rates, both the initial specific capacitance and the rate response of NPCs/Co<sub>3</sub>O<sub>4</sub> are superior to those of CNTs/Co<sub>3</sub>O<sub>4</sub> (Figure 6b). Assuming that a specific capacitance of NPCs ranges from 232 to 139 F g<sup>-1</sup><sup>16c</sup> and the cobalt mass content is around 21% based on the TGA analysis (Figure S7), the corresponding specific capacitance value of Co<sub>3</sub>O<sub>4</sub> nanocrystals at a current rate of 3, 6, 12, 30, and 60 A g<sup>-1</sup> is 1066, 1028, 951, 879, and 721 F g<sup>-1</sup>, respectively (Figure 6b). To our knowledge, these results are among the best electrochemical capacitive values for cobalt oxide electrode materials.<sup>26,27</sup> More importantly, the specific capacitive value is preserved at 721 F g<sup>-1</sup> for a high current density of 60 A g<sup>-1</sup>, equivalent to 67.6% retention of the initial value of 1066 F g<sup>-1</sup>, suggesting that such a prominent capacitive performance can be maintained under a high-power density operation. With a maximum voltage of 0.6 V, a high capacitance value of 333 F g<sup>-1</sup> can be obtained for NPCs/Co<sub>3</sub>O<sub>4</sub> even after 4500 cycles at a current density of 6 A g<sup>-1</sup> (Figure 6c). Apparently, the superior electrochemical properties of NPCs/Co<sub>3</sub>O<sub>4</sub>, which include outstanding capacitive activity and excellent stability, can be reasonably ascribed to the unique composition and structure as discussed above.

The electrochemical results described above unambiguously demonstrate that NPCs/Co<sub>3</sub>O<sub>4</sub> is attractive for application in electrochemical energy storage. Here, NPCs/Pt is exploited to catalyze the electro-oxidation of methanol in alkaline medium, which represents a promising alternative for direct fuel cells.<sup>28</sup> The primary effect of KOH concentration on methanol electro-oxidation illustrated as a linear scan is shown in Figure 7a. For these experiments, the concentration of methanol is set to a constant value of 1 M. In the forward scan region, the anodic peak potential shifts negatively, and the current density, which has been normalized to the electroactive Pt surface area (*j*, Figure S8), increases greatly when the concentration of KOH is increased from 0.1 to 5 M. With the assumption that the electrochemical process is mainly dominated by the diffusion control,<sup>29</sup> the higher concentration of KOH can facilitate the adsorption of OH<sup>-</sup> ions and methanol on Pt active sites, thereby leading to the negative shift of peak potential and the increase of *j*. Furthermore, the cyclic voltammograms of NPCs/Pt in a 5 M KOH solution with a scan rate varying between 2 and 50 mV s<sup>-1</sup> are shown in Figure 7b. The well-defined forward and backward scan peaks indicate the formation of the adsorbed hydroxyl and acetyl groups on the active sites of Pt as well as the rapid removal of the surplus carbonaceous species during

- (26) (a) Shan, Y.; Gao, L. *Mater. Chem. Phys.* **2007**, *103*, 206–210. (b) Ahn, H. J.; Seong, T. Y. *J. Alloys Compd.* **2009**, *478*, L8–L11. (c) Zheng, M. B.; Cao, J.; Liao, S. T.; Liu, J. S.; Chen, H. Q.; Zhao, Y.; Dai, W. J.; Ji, G. B.; Cao, J. M.; Tao, J. *J. Phys. Chem. C* **2009**, *113*, 3887–3894. (d) Wei, T. Y.; Chen, C. H.; Chien, H. C.; Lu, S. Y.; Hu, C. C. *Adv. Mater.* **2009**, *22*, 347–351. (e) Xiong, S. L.; Yuan, C. Z.; Zhang, X. G.; Xi, B. J.; Qian, Y. T. *Chem.–Eur. J.* **2009**, *15*, 5320–5326.
- (27) (a) Liang, Y. Y.; Cao, L.; Kong, L. B.; Li, H. L. *J. Power Sources* **2004**, *136*, 197–200. (b) Cao, L.; Xu, F.; Liang, Y. Y.; Li, H. L. *Adv. Mater.* **2004**, *20*, 1853–1857. (c) Zhou, W. J.; Xu, M. W.; Zhao, D. D.; Xu, C. L.; Li, H. L. *Microporous Mesoporous Mater.* **2009**, *117*, 55–60.
- (28) (a) Tehrani, R. M. A.; Ghani, S. A. *Fuel Cells* **2009**, *9*, 579–587. (b) Bianchini, C.; Shen, P. K. *Chem. Rev.* **2009**, *109*, 4183–4206.
- (29) (a) Kowal, M.; Li, M.; Shao, M.; Sasaki, K.; Vukmirovic, M. B.; Zhang, J.; Marinkovic, N. S.; Liu, P.; Frenkel, A. I.; Adzic, R. R. *Nat. Mater.* **2009**, *8*, 325–330. (b) Peng, Z. M.; Yang, H. J. *Am. Chem. Soc.* **2009**, *131*, 7542–7543. (c) Wang, J. X.; Inada, H.; Wu, L. J.; Zhu, Y. M.; Choi, Y. M.; Liu, P.; Zhou, W. P.; Adzic, R. R. *J. Am. Chem. Soc.* **2009**, *131*, 17298–17302.



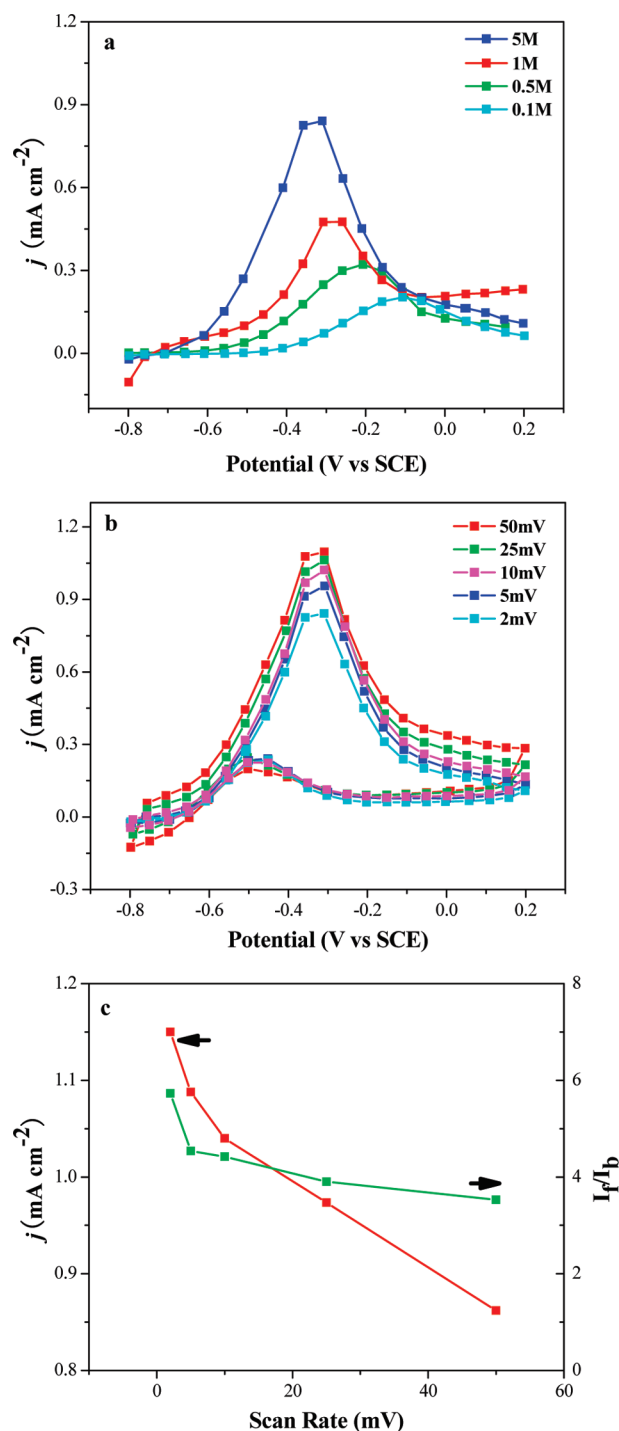


**Figure 7.** (a) Linear scan for the electro-oxidation of methanol on NPCs/Pt in 1 M methanol solution with different KOH concentrations at a scan rate of  $5 \text{ mV s}^{-1}$ . (b) Cyclic voltammograms for the electro-oxidation of methanol on NPCs/Pt in a 1 M methanol + 5 M KOH solution at a scan rate range of 2 to  $50 \text{ mV s}^{-1}$ . (c) Scan rate dependent current density ( $j$ ) and the value of  $I_f/I_b$  for the electro-oxidation of methanol on NPCs/Pt, respectively.

the forward scan.<sup>30</sup> Very interestingly, the current density of the forward scan ( $I_f$ ) is much higher than that of the backward scan ( $I_b$ ). In general, the current density ratio ( $I_f/I_b$ ) is regarded as a critical parameter to estimate the tolerance of the catalyst

(30) (a) Spendelow, J. S.; Wieckowski, A. *Phys. Chem. Chem. Phys.* **2007**, *9*, 2654–2675. (b) Hu, F. P.; Shen, P. K.; Li, Y. L.; Liang, J. Y.; Wu, J.; Bao, Q. L.; Li, C. M.; Wei, Z. D. *Fuel Cells* **2008**, *8*, 429–435.

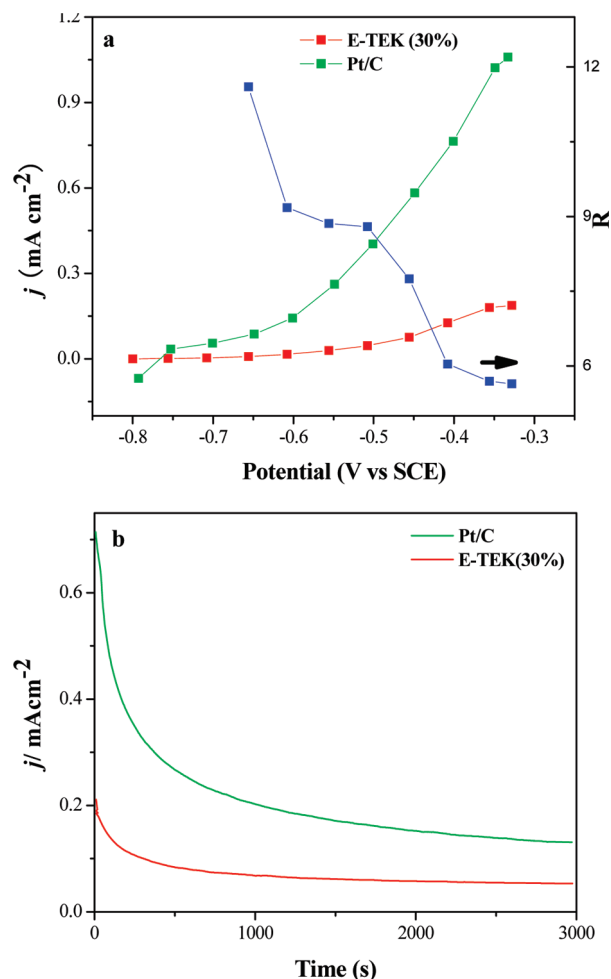


**Figure 8.** (a) Linear scan (left) for the electro-oxidation of methanol on the NPCs/Pt and E-TEK in a 1 M methanol + 5 M KOH solution at a scan rate of  $5 \text{ mV s}^{-1}$ , and the potential-dependent current density ratio  $R$  (right) for NPCs/Pt and E-TEK. (b) Chronoamperometry of methanol oxidation at  $-0.3 \text{ V}$  for the NPCs/Pt and E-TEK in a 1 M methanol + 5 M KOH solution.

to the accumulated intermediate carbonaceous species.<sup>31</sup> As illustrated in Figure 7c, high values of  $I_f/I_b$  ranging from 3.5 to 5.8 are achieved, in contrast to the published data of 1.5 to 2 for Pt/C catalysts.<sup>31</sup> This finding confirms that NPCs/Pt exhibits excellent catalytic efficiency and good tolerance toward poisoning species for the electro-oxidation of methanol.

The linear scans of NPCs/Pt and commercially available E-TEK catalysts with the same Pt mass loading, which have been normalized to the electro-active Pt surface area ( $j$ , Figure S8), are compared in Figure 8a. In the forward scan region, the value of  $j$  toward methanol oxidation of NPCs/Pt is higher than that of E-TEK. The relative enhancement factor  $R$ , which is defined as the ratio of the  $j$  value measured on NPCs/Pt versus on E-TEK, varies from 4.3 to 9.0 depending on the applied electrode potential. Additionally, under a fixed oxidation current density, the corresponding potential value of NPCs/Pt is much lower than that of E-TEK. The typical chronoamperometric

(31) (a) Xu, C. W.; Wang, H.; Shen, P. K.; Jiang, S. P. *Adv. Mater.* **2007**, *19*, 4256–4259. (b) Su, L.; Jia, W. Z.; Schempf, A.; Ding, Y.; Lei, Y. *J. Phys. Chem.* **2009**, *113*, 16174–16180. (c) Sun, Z. P.; Zhang, X. G.; Liang, Y. Y.; Li, H. L. *J. Power Sources* **2008**, *185*, 801–806. (d) Sun, Z. P.; Zhang, X. G.; Liang, Y. Y.; Li, H. L. *Electrochem. Commun.* **2009**, *11*, 557–561.



curve of NPCs/Pt and E-TEK in a mixed solution of 1 M methanol and 5 M KOH solution is recorded, respectively (Figure 8b). Under a given potential of  $-0.3$  V, for the continuous electro-oxidation of methanol on the electrode surface, tenacious reaction intermediates such as CO and HCHO would begin to accumulate if the kinetics of the removal reaction could not keep pace with the methanol oxidation.<sup>28b,32</sup> A slow decay of the peak current for NPCs/Pt with the time scale implies that it has better poisoning tolerance in the alkaline medium than E-TEK (Figure 7c), well consistent with the cyclic voltammogram results. At 3000 s, the corresponding oxidation current value of  $j$  remains at  $0.13 \text{ mA cm}^{-2}$  for NPCs/Pt, much higher than  $0.052 \text{ mA cm}^{-2}$  for E-TEK.

On the basis of the above results and discussions, controlled thermolysis of organometallic precursors has been shown to be an efficient approach for the fabrication of 1D metal–carbon hybrids. Structural characterizations disclose that high-quality  $\text{Co}_3\text{O}_4$  or Pt nanocrystals are well distributed within the 1D nanoporous carbon frameworks. This can be due to the preformation of metallic functionalized polyphenylene backbones that enable control of the nanoarchitectures of carbonaceous and metallic components at the molecular level during the thermal treatment. As a consequence, the obtained 1D NPCs/ $\text{Co}_3\text{O}_4$  and NPCs/Pt materials exhibit superior electrochemical performance in supercapacitors and fuel cells, respectively. This can be rationally attributed to their unique composition and structure. First, the combination of individual metallic nanocrystals with electronically conducting NPCs provides electron superhighways,<sup>33</sup> allowing for rapid and efficient charge transport and leading to an increase in the overall electronic conductivity. Second, the homogeneously distributed metallic nanocrystals on the nanoporous carbon framework of NPCs offer

high-surface-area access to the active sites, thus leading to efficient utilization of the metallic phase for electrochemical energy storage. Third, grafting these metallic nanocrystals onto the mechanically stable NPCs can effectively prevent the agglomeration of electroactive metallic nanocrystals during the continuous electrochemical process.

## Conclusion

In summary, we have successfully demonstrated an in situ fabrication of 1D metal–carbon hybrids incorporating high-quality  $\text{Co}_3\text{O}_4$  or Pt nanocrystals with nanoporous carbon frameworks via a controlled thermolysis of organometallic precursors. Due to their unique composition and architecture, NPCs/ $\text{Co}_3\text{O}_4$  and NPCs/Pt display excellent electrochemical performances in supercapacitor and fuel cell devices, respectively. Our findings provide a deeper understanding of the concept of organometallic precursor-controlled thermolysis as a straightforward processing protocol for the buildup of thermally stable and structurally ordered 1D metal–carbon hybrids. This approach enables the promising prospect that a variety of functional hybrid materials with intriguing properties will be accessible for widespread applications in a range of lithium ion batteries, micro- or nanotransistors, and magnetic memory devices.

**Acknowledgment.** This work was financially supported by the Max Planck Society through the program ENERCHEM, National Natural Science Foundation of China (No. 50701023). Y.L. gratefully acknowledges the Alexander von Humboldt Stiftung for a research fellowship. M.G.S. thanks the “Graduate School Materials Science in Mainz” for a scholarship.

**Supporting Information Available:** Synthetic route and MALDI-TOF mass spectra of Co-Cp and Pt-BpCp; XRD, DSC, TGA, and electrochemical active surface spectra. These materials are available free of charge via the Internet at <http://pubs.acs.org>.

JA106612D

- (32) Mayrhofer, K. J. J.; Hartl, K.; Juhart, V.; Arenz, M. *J. Am. Chem. Soc.* **2009**, *131*, 16348–16349.
- (33) (a) Wang, D. W.; Li, F.; Liu, M.; Lu, G. Q.; Cheng, H. M. *Angew. Chem., Int. Ed.* **2008**, *47*, 373–376. (b) Zhang, H.; Cao, G.; Wang, Z. Y.; Yang, Y. S.; Shi, Z. J.; Gu, Z. N. *Nano Lett.* **2008**, *8*, 2664–2668. (c) Hu, C. H.; Chang, K. H.; Lin, M. C.; Wu, Y. T. *Nano Lett.* **2006**, *6*, 2690–2695.